Physics of Plasmas ARTICLE pubs.aip.org/aip/pop

Trichel pulse characteristics and mechanism of negative corona discharge in sub-millimeter gaps

Cite as: Phys. Plasmas **30**, 063901 (2023); doi: 10.1063/5.0145301
Submitted: 5 February 2023 · Accepted: 9 May 2023 ·
Published Online: 1 June 2023

Zhi Sun,[1] Zhuo Kai Shao,[1] Xing Sun,[1] and Wei Feng Sun[2,a)]

AFFILIATIONS

[1]Key Laboratory of Engineering Dielectrics and Its Application, Ministry of Education, School of Electrical and Electronic Engineering, Harbin University of Science and Technology, Harbin 150080, China
[2]School of Electrical and Electronic Engineering, Nanyang Technological University, Singapore 639798, Singapore

[a)]**Author to whom correspondence should be addressed:** weifeng.sun@ntu.edu.sg

ABSTRACT

A negative corona discharge system of a needle-plate electrode suitable for sub-millimeter gaps is established to investigate Trichel pulse characteristics of negative corona discharge, in which an optical acquisition system is especially applied to timely observe a discharging corona. Electrostatics–hydrodynamics coupling simulations of air discharging in 100 μm-gaped needle-plate electrodes are performed to elucidate the micro-physical process of negative corona discharge. The impact ionization coefficient used for simulations and the experimentally recorded images of discharge corona are combined to characterize the active region of secondary electron emission. Dynamical distribution and transport of the charged particles are analyzed from multiphysics simulations to explain the microscopic mechanism for various stages of Trichel pulses. Even though the corona front near the plate electrode maintains a high rate of collision ionization and secondary electron excitation, the needle tip corona has not reached the threshold electric field of electron avalanche required for glow discharge, as manifested by discharge sawtooth waves comprised of corona and glow components. The amplitude and frequency of Trichel pulses increase, respectively, with impact ionization and secondary electron emission, which is evidently dependent on attachment coefficient and anion mobility. A higher attachment coefficient will lead to a significant reduction in amplitude of Trichel pulses. The present study provides a theoretical basis and experimental verification for micrometer discharges, which is the key point of insulation protections in microelectromechanical systems.

I. INTRODUCTION

Gas corona discharge generated at low-temperature is a paradigm of non-equilibrium plasma discharge.[1] Corona discharge occurs near the needle electrode with a high tip curvature where an electric field reaches an adequate intensity to cause electrical breakdown of gas dielectrics. Air micro-gap discharge through electronic-excitation, ionization, charge migration, and diffusion produces a large number of free moving electrons and ions as plasma.[2–4] Compared with positive corona discharge, the negative corona discharge represents definite regularity where high scientific interest resides in Trichel pulses. Given high randomness of gas discharge and extremely high requirement of electrode parameters, studying on the sub-millimeter air-gap discharge mechanism is still a daunting challenge until now.[5,6]

The three-dimensional model of negative corona discharge based on fluid dynamics of applying finite-element and flux-correct-transport (FE-FCT) is capable of calculating charge distribution in a discharge gap under atmospheric pressure but not successful to simulate a sequence of consecutive Trichel pulses.[7] By introducing impact ionization into the hybrid numerical model of coupling fluid dynamics and chemical reactions, the transport mechanism of charged particles in needle-plate corona discharge was well elucidated in detail, which can be utilized to analyze impact ionization probability and ion density in electrode sheath layers and the plasma region.[8] In addition to impact ionization, the secondary electron emission and electron temperature are necessary to be incorporated for quantitatively analyzing electric field and charge density of Trichel pulses.[9–11] The newly updated FE-FCT method is successful of evaluating secondary emission and ion mobility in continuously sequenced Trichel pulses.[12] With the improved control equations of negative corona discharge to quickly solve photo-ionization using the Helmholtz method, the effect of photo-ionization on negative corona discharge was represented especially for various temperatures and air pressures.[13] Drift-diffusion

finite-element simulations of coupling photo-ionization, fluid dynamics, and electrostatics enable comprehensive analyses of electron distribution, electric field, and current density on plate surface.[14]

The dependence of corona discharge characteristics on needle-plate gaps has been extensively studied over the years, with a growing interest in investigating the effect of gap distance on corona discharge characteristics, such as corona discharge inception voltage, pulse waveform development, and optical emission spectrum.[15,16] Recent studies highlight the importance of understanding the dependence of corona discharge characteristics on needle-plate gaps, particularly in sub-mm scales, which is crucial for the design and optimization of various applications that rely on corona discharges, such as electrostatic precipitation, ozone generation, and electrostatic spraying.[17–19] Therefore, the dependence of corona discharge characteristics on the needle-plate gaps in sub-mm scales is a crucial factor in understanding the behavior of corona discharges.

For the present study, in high interest of revealing characteristics and mechanism of negative corona discharge in sub-millimeter (100–500 μm) gaps, we rely on an image acquisition system and electrostatic-hydrodynamic multiphysics finite-element simulations to real-timely observe and snoop microscopically corona discharge of Trichel pulse. The plasma model suitable for negative corona discharge in a 100 μm gap is proposed for electrostatic field-fluid dynamics finite-element simulations. The coupled CCD optical image acquisition system is employed, and Trichel pulse volt-ampere characteristics are tested in real-time to elucidate the negative corona discharge process in sub-millimeter gaps.

II. EXPERIMENTAL AND SIMULATION METHODS

A. Experimental platform

The discharge system includes a DC high-voltage power supply, protection resistance, needle-plate electrode, oscilloscope, high-voltage probe, sampling resistance, and high-voltage microampere meter, as shown in Fig. 1. The DC power supply applies a negative DC voltage to the needle-plate electrode by protection resistance, which means the needle electrode is applied by negative voltage while the plate electrode is grounded. The plate electrode is connected with the three-axis micrometer-resolved displacement platform to accurately control needle-plate distance (air-gap) of 1 μm resolution in 0–500 μm range. Trichel pulses of electric current in μA resolution are measured by testing the pulse voltage of ground resistance (R2) using voltage oscilloscope, in which the low voltage probe is used for sampling resistance (R1) and the high-voltage probe is used for testing discharge voltage between the needle and plate electrodes, as shown in Fig. 1. The coupled CCD optical microscope is setup with the objective lens at ~5 cm distance from needle-plate gap to observe the development of corona discharge, which is also utilized for calibrating needle-plate distance.

B. Electrostatics-hydrodynamic coupling simulation

Hydrodynamics simulations of negative corona discharge mainly focus on discharge gaps of 6 or 3.3 mm as reported recently.[7] To investigate characteristics and the microscopic mechanism of Trichel pulse in sub-millimeter gap negative corona discharge, the essential physical parameters of the fluid dynamics model are improved specially for simulations of 100 μm-gap needle-plate discharge.

1. Fluid discharge control equation and boundary condition

The dynamical model represents impact ionization, recombination and secondary emission of electrons with ions, and electrode adsorption to simulate the generation or fading away of the charged particles without considering chemical reaction of air molecules, as implemented by Plasma modules of COMSOL Multiphysics 6.0, which is specified to resolve the coupled Boltzmann diffusion and Poisson electrostatic equations. Geometrically, a two-dimensional axis-symmetric model is established with identical size and shape of needle-plate electrode as experiments, for which the curvature radius of needle electrode and the needle-plate distance are set to 2 and 100 μm, respectively. Due to the high electric field strength approaching 10^8 V/m in sub-millimeter gaps causing over-enhancement of electron impact ionization, the conventional Morrow discharge parameters used in fluid dynamics models cannot represent Trichel pulse in sub-millimeter scale.[7] Accordingly, in the present study,

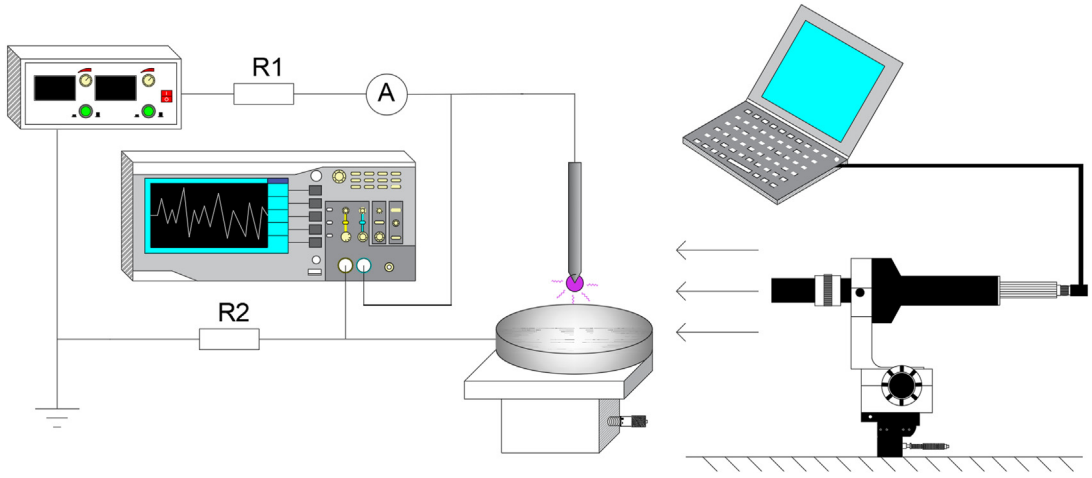

FIG. 1. Schematic equipment for corona discharge in air-gap of the needle-plate electrode.

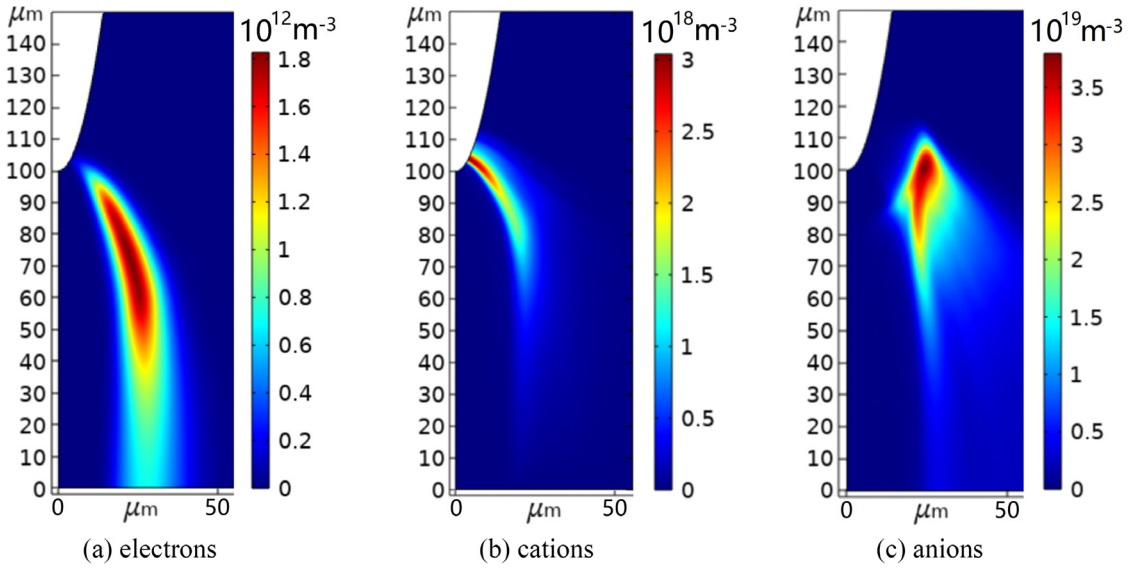

FIG. 2. The charged article density in color contours.

the discharge parameters are modified suitable for 100–500 μm needle-plate gaps, in which Trichel pulse waveform arises in simulations by specifying secondary electron emission coefficient to 0.035, as shown in Fig. 2. After specifying discharge parameters, we found that varying needle tip curvature and model size will not significantly degrade simulated Trichel pulse characteristics, and the particle density distribution remains almost unchanged. As shown in Figs. 2(a) and 2(b), only the cations rather than the anions are distributed on the tip surface of needle electrode to generate the electrons which continuously migrate far away from the needle tip region toward plate electrode, implying that the ionization reaction at needle electrode is dominated by the cations impacting on needle surface to produce secondary electrons. It has been verified from various experimental reports that the field emission can dominate air discharge and breakdown merely for needle-plate gap of <5 μm, while the Thomson theory is still valid to explain the air discharges in needle-plate gap of >10 μm.[20,21]

Since secondary electrons are mainly derived from cations impacting on the surface of the cathode needle under the electric field, the region of secondary electron emission is specified according to the observed discharge corona in radius of 5 μm around needle tip as

$$\gamma = \begin{cases} 0.01, & z < 105\,\mu\text{m}, \\ 0, & z > 105\,\mu\text{m}, \end{cases} \tag{1}$$

where γ denotes the secondary electron emission coefficient and z indicates the axial direction of the needle-plate electrode. Preliminary simulation results of 100 μm-gap discharge demonstrate that electric field strength in the discharge region approaches 10^7–10^8 V/m, which is 10–100 times higher than that of millimeter gap discharge. Thus, electrons will obtain a remarkably higher energy with a higher impact ionization in corona discharge of 100 μm-gap than that of millimeter gap. Therefore, the calculation formula of impact ionization is improved by

$$\alpha/p = Ae^{-Bp/E}, \tag{2}$$

where $A = 11.25$ m^{-1} Pa^{-1} and $B = 273.8$ V·m^{-1} Pa^{-1} under room temperature and normal pressure, which leads to simulation results agreeing well with experiments. The physical parameter set adopted for air discharge simulations is listed in Table I.[7,22,23] For boundary specifications, secondary electron yield on the needle electrode surface is calculated as follows:

$$\Gamma_e = \gamma N_p \mu_p |\vec{E}|, \tag{3}$$

TABLE I. Discharge parameters adopted for multiphysics finite-element simulations.

Physical parameter	Value	Unit
Impact ionization coefficient α	$11 \times 10^5 \exp(-2.8 \times 10^7/E)$	(1/m)
Attachment coefficient η	$0.3 \times 10^3 \exp(-2.5 \times 10^6/E)$	(1/m)
Electron mobility μ_e	$10^{3.524} \times (10^{21} \times E/N_{neu})^{0.782}$	[m^2/(V s)]
Cation mobility μ_p	2.43×10^{-4}	[m^2/(V s)]
Anion mobility μ_n	1.35×10^{-5}	[m^2/(V s)]
Electron diffusion coefficient D_e	0.18	(m^2/s)
Cation diffusion coefficient D_p	0.028×10^{-4}	(m^2/s)
Anion diffusion coefficient D_n	0.043×10^{-4}	(m^2/s)
Recombination coefficient of cation and anion β_{np}	1×10^{-13}	(m^3/s)
Recombination coefficient of electron and cation β_{ep}	2×10^{-13}	(m^3/s)

TABLE II. Boundary conditions for the needle-plate discharge model. N_{neu} denotes neutral particle density determined by temperature (293.15 K) and air pressure (normal).

Controlling equation	Needle/air boundary	Plate/air boundary	Peripheral boundary
Electron transport	Inflow flux $\Gamma_e = \gamma N_p \mu_p \lvert\vec{E}\rvert$	Outflow flux $-\vec{n}\cdot D_e \nabla N_e = 0$	Outflow without inflow $\begin{cases} -\vec{n}\cdot D_e\nabla N_e = 0; & \vec{n}\cdot\mu_e\lvert\vec{E}\rvert \geq 0 \\ N_e = 0; & \vec{n}\cdot\mu_e\lvert\vec{E}\rvert \leq 0 \end{cases}$
Cation transport	Outflow flux $-\vec{n}\cdot D_p \nabla N_p = 0$	Constant density $N_p = 0$	Outflow without inflow $\begin{cases} -\vec{n}\cdot D_p\nabla N_p = 0; & \vec{n}\cdot\mu_p\lvert\vec{E}\rvert \geq 0 \\ N_p = 0; & \vec{n}\cdot\mu_p\lvert\vec{E}\rvert \leq 0 \end{cases}$
Anion transport	Constant density $N_n = 0$	Outflow flux $-\vec{n}\cdot D_n \nabla N_n = 0$	Outflow without inflow $\begin{cases} -\vec{n}\cdot D_n\nabla N_n = 0; & \vec{n}\cdot\mu_n\lvert\vec{E}\rvert \geq 0 \\ N_n = 0; & \vec{n}\cdot\mu_n\lvert\vec{E}\rvert \leq 0 \end{cases}$
Poisson	Electrostatic potential $V = V_{app}$	Grounded $V = 0$	Zero charge $\vec{n}\cdot(\varepsilon\vec{E}) = 0$

where Γ_e signifies flux of secondary electron emission. Cations outflow from the needle cathode without anions, while electrons and anions outflow from the surface of the ground plate electrode, and all the charged particles are specified to flow out from the periphery boundary, as shown by boundary flux expressions listed in Table II.

2. Element meshing and initial condition

Finite-element meshing near needle tip is refined with minimum and maximum sizes of 0.03 and 0.06 μm, respectively, in which meshing growth rate and curvature factor are set to 1.1 and 0.2, respectively. Domain regions away from needle electrode are meshed with

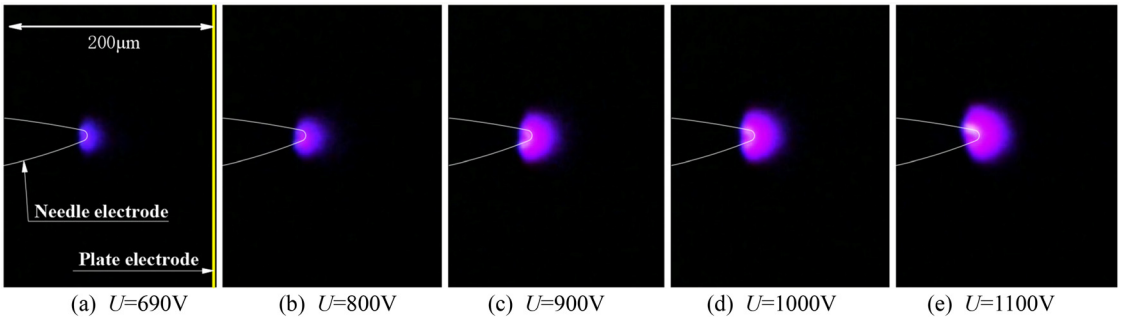

FIG. 3. Images of negative corona discharge in 100 μm air-gap.

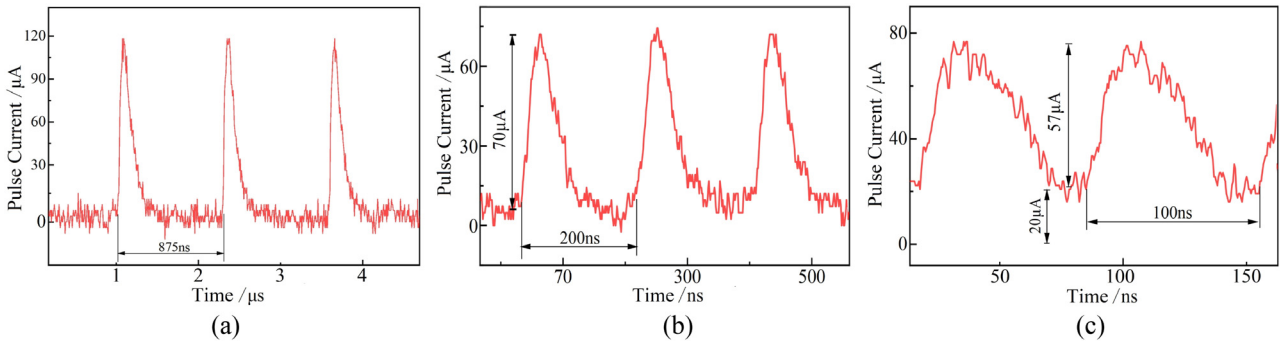

FIG. 4. Pulse waveforms of negative corona discharges in 100 μm air-gap: (a) initial stage of Trichel pulse at $U_A = 690$ V, (b) middle stage of Trichel pulse at $U_A = 800$ V, and (c) Trichel pulse sawtooth waves at $U_A = 1100$ V.

minimum 0.1 μm and maximum 1.2 μm element sizes. Initial densities of the charged particles near needle electrode surface are set by ignoring anion density and applying Gaussian distribution for electrons and cations as

$$N_{e,p} = N_{max} \times \exp\left(-\frac{(r-r_0)^2}{2s_0^2} - \frac{(z-z_0)^2}{2s_0^2}\right), \quad (4)$$

where $N_{max} = 10^{16}$ m^{-3}, $r_0 = z_0 = 5$ μm, and $s_0 = 25$ μm.

III. RESULTS AND DISCUSSION

A. Sub-millimeter-gap negative corona discharge characteristics

The development process of millimeter gap negative corona discharge is mainly divided into three stages: Townsend discharge, Trichel pulse, and pulse-free stage. However, for sub-millimeter gap, the negative corona discharge is considerably distinct from millimeter gap due to a magnitude smaller of electrode spacing and needle tip curvature radius. We adopt a negative voltage DC source of 500–1200 V with a linearly boost rate of 5 V/s to observe discharge corona development of 100 μm air-gap by CCD optical microscope, as shown in Fig. 3. Simultaneously, pulse waveforms for different periods of 100 μm-gap negative corona discharge are tested with the results being shown in Fig. 4. When U_A approaches 690 V, the electric field near needle approaches threshold strength of self-sustaining discharge, presenting discharge current of 10^{-6}A, so that a stable blue corona appears at needle tip in conversion from Townsend to Trichel pulses, as shown in Figs. 3(a) and 4(a). While $U_A = 800$–1000 V, the negative corona at the needle tip changes from blue to blue-purple colors, implying the middle and late stage of Trichel pulse discharge, as shown in Figs. 3(b), 3(c) and 4(b). Ultimately, as U_A=1000–1100 V, it enters the period of Trichel pulse sawtooth wave, as shown in Figs. 3(d), 3(e) and 4(c). Expansion of negative corona discharge region in sub-millimeter gaps concentrates in Trichel pulse period, without glow discharge such as occurring in millimeter gap. Because discharge spacing

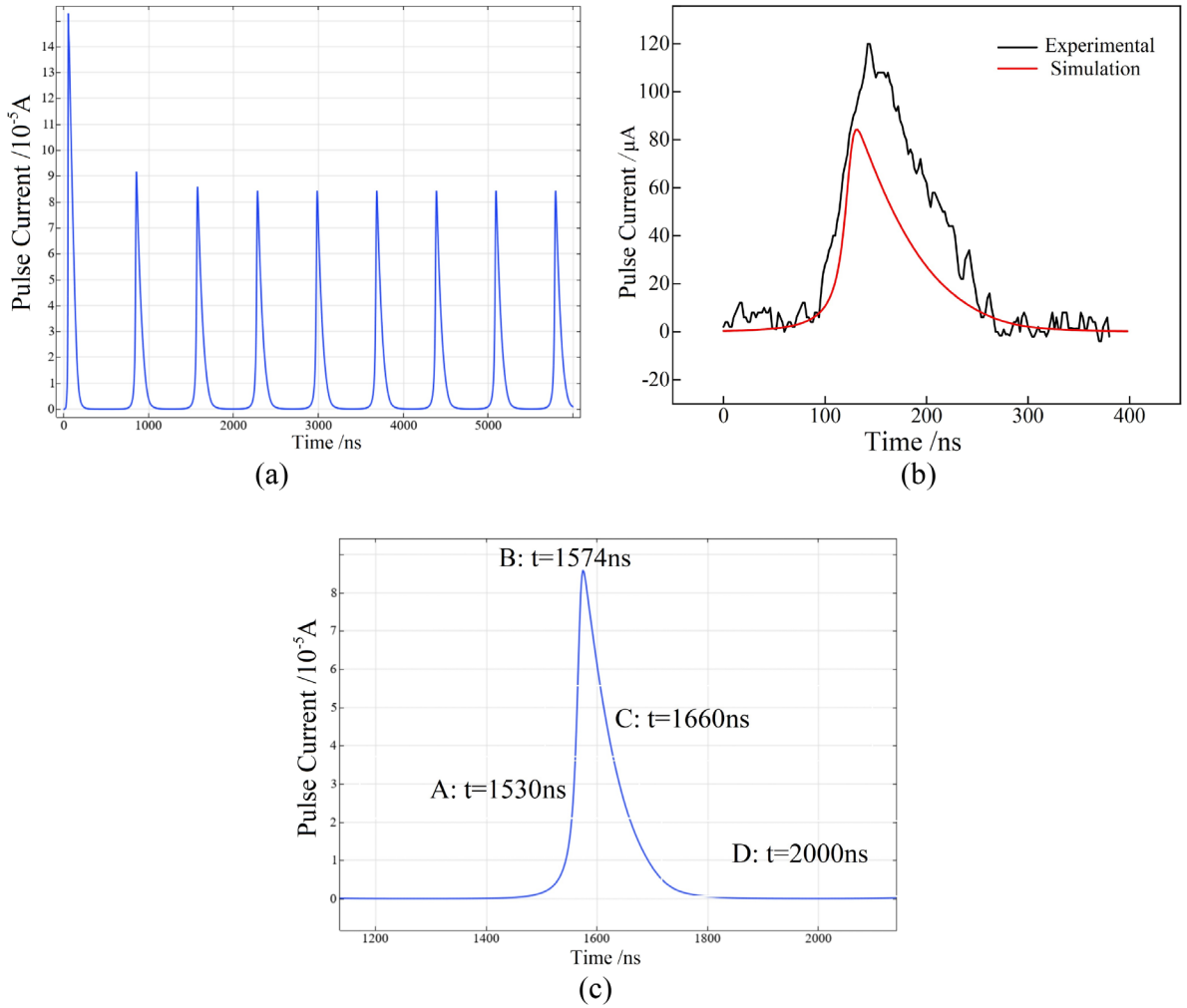

FIG. 5. (a) Current sequence from 100 μm air-gap discharge simulation; (b) Trichel pulse simulation and experimental results; (c) schematics of the third Trichel pulse.

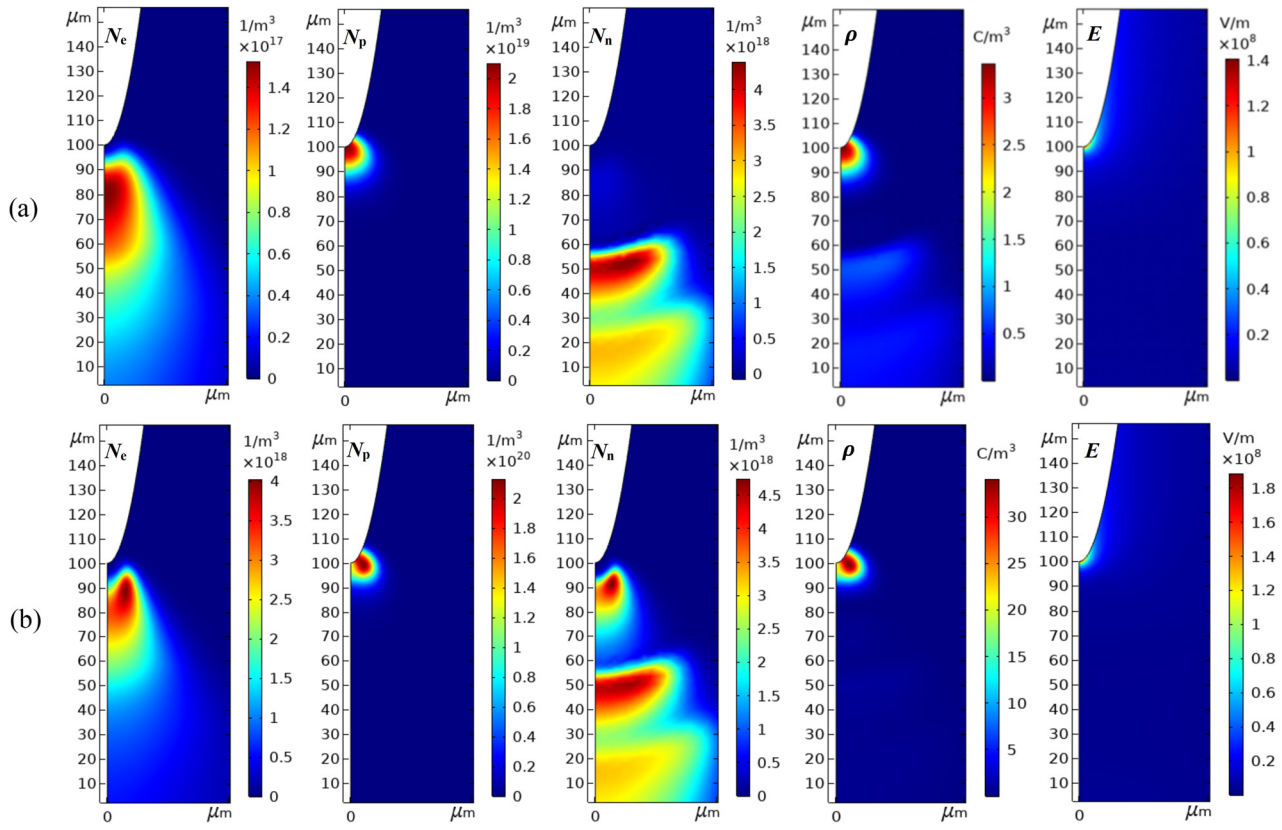

FIG. 6. The charged article density and electric field in discharge region at stages of (a) A and (b) B.

is too small scaled in sub-millimeters, the negative corona discharge directly develops into stream discharge.

Initial pulses characterize the typical Trichel waveform of a short rising edge ($t_r = 40$ ns), the very long falling edge, and waiting time, while pulse period approaches 875 ns with a current amplitude of 120 μA. When $U_A = 800$ V progresses to the middle stage of the Trichel pulse, the pulse period decreases sharply to 200 ns, and the current amplitude drops to 70 μA, but the rise edge remains unchanged, as shown in Fig. 4(b). After the voltage increases to 1100 V, the corona develops into intensive discharge of sawtooth waves without waiting time, as shown in Fig. 4(c), while pulse period and amplitude continue decreasing to 100 ns and 57 μA, respectively. In particular, when 100 μm-gap negative corona discharge develops almost to stream discharge, the pulse current deviates overall with a plate current of ~20 μA.

At the beginning of the Trichel pulse, the negative charges have not attained a sufficient density to effectively cancel electric field near the needle tip, and the positive charges dominate in discharge air-gap, which leads to a higher amplitude of negative corona discharge. Due to accumulations of the charged particles in discharge gap, the charge dissipation time increases, and the subsequent pulses are inhibited, as indicated by a lower Trichel pulse frequency. As the applied voltage increases, the accumulation of negative charges brings down electric field strength in discharge gap, thus reduces pulse amplitude. The conversion in each stage of negative corona discharge shows a jump of pulse amplitude, especially in the middle and late stages of Trichel pulse. For negative sub-millimeter gap, the transition from corona to glow discharges is vague or not even arising, and sawtooth pulse waves retain in company with a conspicuous

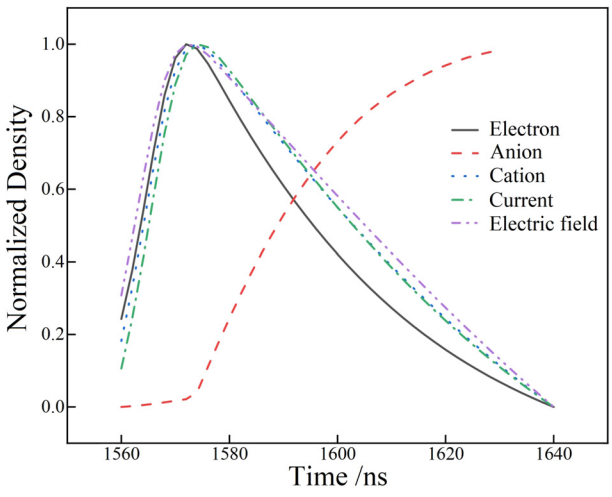

FIG. 7. Normalized densities of electrons, anions, and cations; discharging current; and electric field.

plate current before reaching stream discharge. Unlike in millimeter gaps, the Trichel pulse waveform of sub-millimeter gap discharge shows a sawtooth shape accompanied by a background current without any pulseless stage. Therefore, in contrast to millimeter gaps, the corona discharge in sub-millimeter gaps cannot transition to the glow discharge stage, which will directly transform into streamer discharge.

B. Fluid dynamic discharge simulations

1. Current and charge density of Trichel pulse

Trichel pulse series of negative corona discharge by applying 690 V to 100 μm-gap needle-plate electrode are simulated with the results being shown in Fig. 5(a). At initial discharge, the first pulse is unaffected by charges generated in air-gap, while pulse amplitude after the third pulse varies gradually to a converged value of 86 μA. The waveform, rise edge, and frequency of Trichel pulses from simulation are comprehensively consistent with experimental results, as shown in Fig. 5(b) (only one wave is presented). As a typical Trichel pulse, the third of simulated pulse sequence could be divided into four stages: (A) initial pulse stage, (B) electric field suppression stage, (C) anion migration stage, and (D) pulse discharge preparation stage, as shown in Fig. 5(c).

At the initial pulse stage, the charge density in discharge gap reaches 3.36 C/m^3, which is not sufficient to distort the electric field of causing electron impact ionization, as shown in Fig. 6(a). At $t = 1530$ ns, when the electric field strength of 1.39×10^8 V/m exceeds threshold of engendering corona discharge to generate multiple ions by electron impact ionization, the cation cloud is concentrated onto needle electrode, while the electron and anion cloud begins to drift toward plate electrode under divergent electric field, which enhances electric field near needle electrode. Meanwhile, the anion cloud remains a lower charge density than cation cloud, accounting for the discharge dominated by impact ionization. During the electric field suppression stage of B, both the densities of electrons and cations reach maximum values, as shown in Fig. 6(b), in which anions accumulate in the migration region near needle tip to shrink the ionization region and decrease electric field strength near needle electrode. The normalized densities of electrons, anions, and cations; discharging current; and electric flux at the B stage (as shown in Fig. 7) indicate that electron concentration and electrical current have begun to decline before the electric field strength increasing evidently, as a manifestation of the sufficient anion density bearing on electric field strength in the discharge region. Although the maximum electric field near the needle electrode has approached to 10^7–10^8 V/m, which is close to the threshold of field emission for an ordinary metal electrode, it is generally valid for the

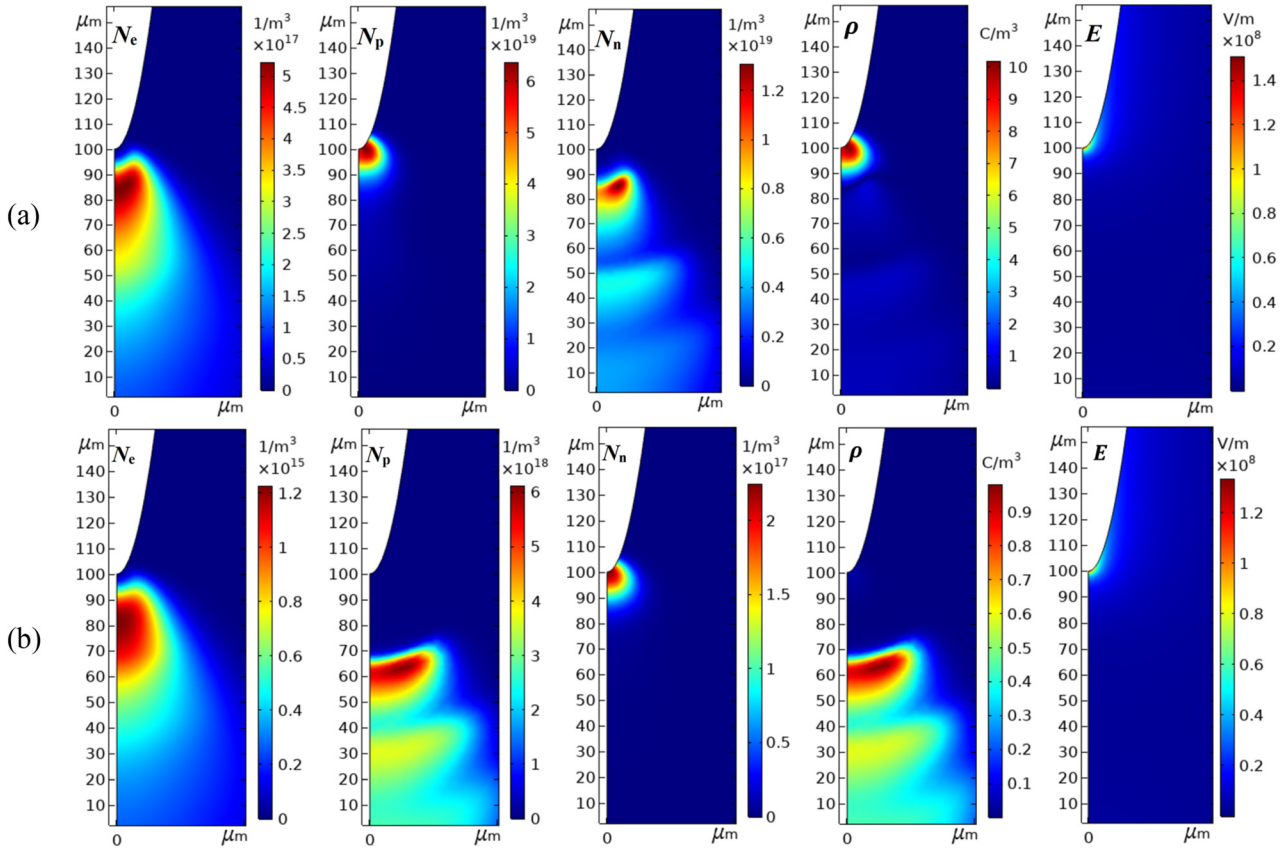

FIG. 8. The particle density and electric field distribution in the discharge region at stages of (a) C and (b) D.

negative corona discharge in a needle-plate gap smaller than 30 μm. Thus, in the present study, the field emission is ignored for the negative corona discharge of 100–500 μm needle-plate gaps.

During the anion migration stage, the electric field near needle has been suppressed to be incapable of initializing electron impact ionization, while electron recombination leads to significant reduction of anion concentration in the discharge region, as shown in Fig. 8(a). Before cation cloud is fully absorbed by the ground plate electrode, the cation and anion clouds retain close enough to bate the Laplace electric field in the middle of discharge gap, implying that Trichel pulse discharge entering D stage, as manifested by electrons and cations approaching to minimum concentrations in Fig. 8(b). Anion cloud drifting toward plate electrode under electric field accounts for the enhanced electric field near needle tip of initializing secondary electron emission and restoring pulse waveform. Therefore, it is not necessary of introducing new pulse to wait anion cloud being completely released by plate electrode, demonstrating multiple anion clouds existing in discharge gap whose number increases as discharge prolongation. After anion clouds moving through the whole gap, the electric field intensity in discharge region remains unchanged, leading to a few changes in Trichel pulse amplitude.

2. Impact ionization and electrode adsorption

Trichel pulse current amplitude and frequency are more dependent on electron impact ionization than on electrode adsorption of the charged particles, as shown in Figs. 9(a) and 9(b). The higher coefficients of impact ionization and adsorption lead to the appreciable decrease and increase in Trichel pulse rise edge, respectively, as shown in Fig. 9(c). Anion adsorption on needle surface causes a higher anion density near needle electrode to suppress electron emission, which reduces Trichel pulse amplitude and enhances electric field at needle tip that subsequently accounting for the increase in Trichel pulse frequency, as shown in Fig. 9(d).

Impact ionization of engendering electrons and cations occurs mainly at the needle tip, after which the rendered electrons migrate to

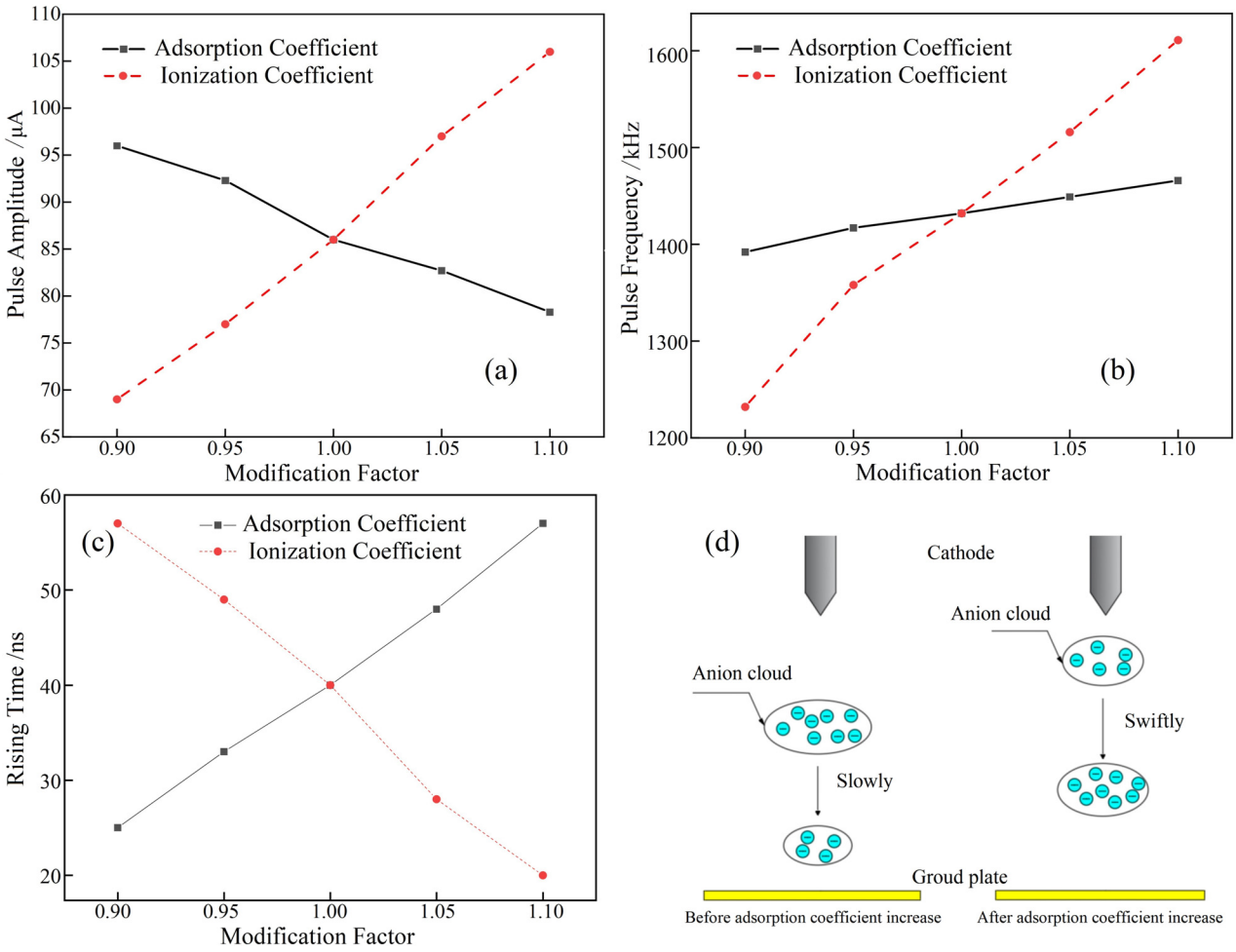

FIG. 9. Impact ionization and attachment coefficients bearing on (a) amplitude, (b) frequency, (c) rise edge of Trichel pulses, and (d) schematic correlation of attachment coefficient with anion cloud in the discharge region.

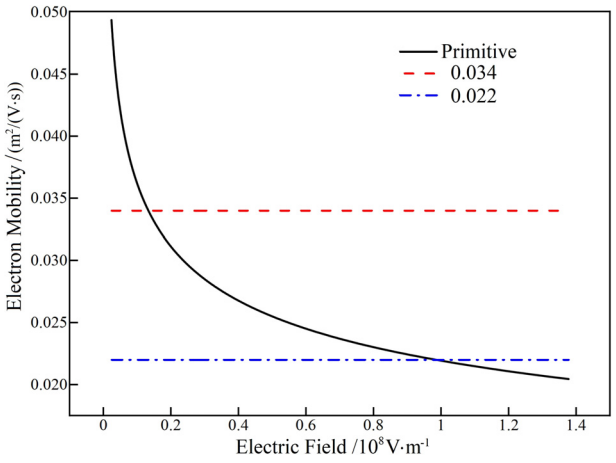

FIG. 10. Comparison of the two constant electron mobilities with primitive electron mobility.

the plate electrode while the generated cations with a higher mass remain stationary as supposed. Consequently, cations will accumulate and enhance electric field around needle surface. If impact ionization coefficient is raised, the cation cloud can enhance electric field near needle, exceeding electric field suppression of anion cloud, which results in a higher Trichel pulse amplitude and expedites anion drifting toward plate electrode that facilitates electrons and cations to accumulate near needle electrode, as manifested by a higher Trichel pulse frequency.

3. Charge mobility

Electron mobility, which is decaying with increasing electric field strength, is comparatively set as constant values of 0.034 and 0.0220 to investigate its responsibility to Trichel pulse, as shown in Fig. 10, and the negative corona discharge characteristics with these different electron mobilities are listed in Table III. A higher electron mobility results in a lower Trichel pulse frequency or amplitude, while rise edge of Trichel pulse will be raised. As shown in Fig. 11(a), Trichel pulse amplitude is almost unchanged with cation mobility but response highly to anion mobility. In contrast, Trichel pulse frequency increases significantly with the increased ion mobility, as shown in Fig. 11(b). Nevertheless, Trichel pulse rise edge is stable to anion mobility but remarkably increases with cation mobility, as shown in Fig. 11(c). In the Trichel pulse discharge preparation stage, the impacting process of cations on needle surface could be exacerbated by improving cation mobility, which means a higher secondary electron emission rate of needle tip results in a shorter time of forming subsequent Trichel pulse, as shown in Fig. 11(d).

TABLE III. Influence of electron mobility on Trichel pulses.

Electron mobility $[m^2/(V\ s)]$	Pulse amplitude (μA)	Pulse frequency (kHz)	Rising time (ns)
$10^{3.523}\times(10^{21}\times E/N_{neu})^{0.782}$	86	1432	40
0.022	60	1814	37
0.034	58	1760	44

The anion cloud migrating in the discharge gap does not rely on secondary electron emission and electron avalanche processes near needle electrode, thus contributing nothing to the rise edge of Trichel pulse. Meanwhile, Trichel pulse frequency depends intensively on anion mobility. The faster anion cloud migrating away from needle electrode, the shorter of time required for electric field to restore strength near needle tip for generating subsequent electron avalanche, implying that Trichel pulse frequency will increase with anion mobility.

4. Secondary electron emission

As indicated by the current amplitude, frequency, and rise edge of the Trichel pulse in dependence on secondary electron emission coefficient γ in Figs. 12(a) and 12(b), both amplitude and frequency increase with γ up to 93 μA and 1618 kHz at $\gamma = 0.012$, respectively. The Trichel pulse rise edge is accelerated by twofold when γ rises from 0.008 to 0.012, as shown in Fig. 12(c). Maintaining a high value of γ is a necessary condition for self-sustaining discharge in negative corona to generate secondary electrons by cations impacting on cathode surface. A higher γ will lead to the higher electron and cation concentrations near needle electrode, which accounts for amplitude increase and rise edge decrease in Trichel pulse. Accordingly, a higher cation concentration near the needle electrode can intensify the electric field between the cation cloud and needle tip, leading to expeditions in impact ionization and subsequent pulse formation, which accounts for the shortage of preparation stage and the promotion of Trichel pulse frequency.

IV. CONCLUSION

A needle-plate test system is built up with a real-time image acquisition system to study characteristics and mechanism of negative corona discharge in a 100 μm air-gap, in which voltage–current curves and discharge corona images of Trichel pulses are analyzed in combination with electrostatic-hydrodynamic coupling finite-element simulations. It is found that the discharge mode between corona and glow discharges has been inhibited or even absent. According to electron and ion mobility, charge density, and electric field strength, the development of Trichel pulses is demarcated into initial pulse, electric field suppression, anion migration, and discharge preparation stages. The initial stage of discharge pulses is dominated by impact ionization, which renders cation cloud to promote electric field strength near needle electrode, thus expediting pulse formations. During the electric field suppression stage, the anion cloud migrates toward the plate electrode in attenuation of the needle electrode electric field, while electron and cation densities and electric field strength start to decline. At the anion migration stage, the anion cloud accumulated in the discharge region and the cations near needle electrode are neutralized to mitigate Laplace electric field in the discharge center. After the anion cloud drifts into plate electrode, the electric field intensity at the needle tip recovers to exacerbate secondary electron emission, identifying that Trichel pulses have developed into discharge preparation stage. Impact ionization, secondary electron emission, and anion mobility determine the amplitude and frequency of Trichel pulse currents. It should be noted that adsorption interaction between electrode surface and discharging particles can simultaneously increase frequency and

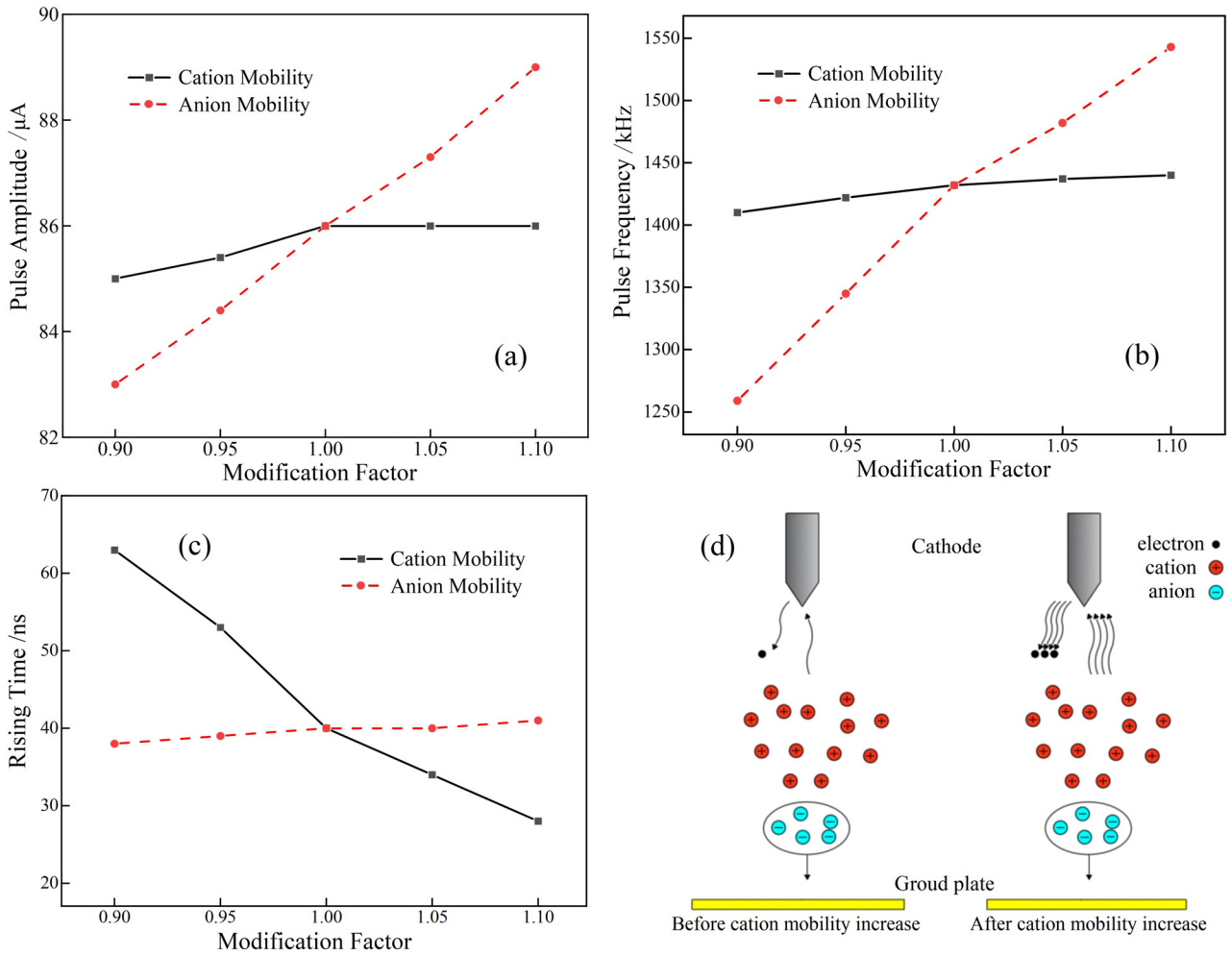

FIG. 11. Cation and anion mobility bearing on the (a) amplitude, (b) frequency, (c) rise edge of Trichel pulse, and (d) schematic correlation of cation mobility with secondary electron emission from needle tip.

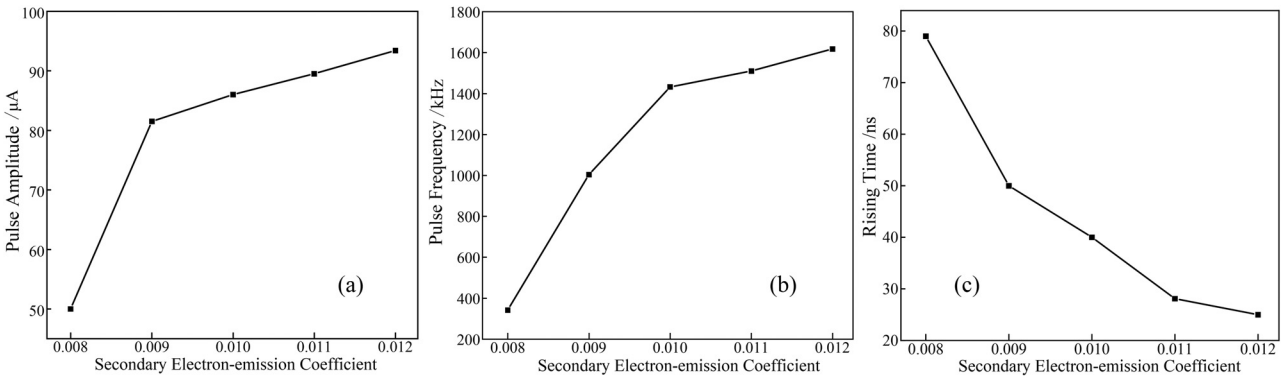

FIG. 12. Secondary electron emission coefficient and anion mobility for Trichel pulse: (a) amplitude, (b) frequency, and (c) rise edge.

rise edge of Trichel pulses while abating amplitude currents of Trichel pulses.

AUTHOR DECLARATIONS

Conflict of Interest

The authors have no conflicts to disclose.

Author Contributions

Zhi Sun: Conceptualization (equal); Methodology (equal); Resources (equal). **Zhuo Kai Shao:** Software (equal); Validation (equal). **Xing Sun:** Data curation (equal); Formal analysis (equal). **Wei Feng Sun:** Investigation (equal); Writing – original draft (equal); Writing – review & editing (equal).

DATA AVAILABILITY

The data that support the findings of this study are available from the corresponding author upon reasonable request.

REFERENCES

[1]C. P. Hsu, N. E. Jewell-Larsen, I. Krichtafovitch, and V. A. Mamishev, "Heat-transfer-enhancement measurement for microfabricated electrostatic fluid accelerators," J. Microelectromech. Syst. **18**(1), 111–118 (2009).

[2]L. Huang, S. Yang, S. Liu, Q. Wang, and Y. Zhu, "Removal of NO_2 produced by corona discharge in indoor air cleaning," J. Adv. Oxidation Technol. **12**(2), 238–241 (2009).

[3]D. Mariotti and R. M. Sankaran, "Microplasmas for nanomaterials synthesis," J. Phys. D: Appl. Phys. **43**(32), 323001 (2010).

[4]T. von Woedtke, A. Schmidt, S. Bekeschus, K. Wende, and K. D. Weltmann, "Plasma medicine: A field of applied redox biology," In Vivo **33**(4), 1011–1026 (2019).

[5]J. G. Eden, S. J. Park, C. M. Herring, and J. M. Bulson, "Microplasma light tiles: Thin sheet lamps for general illumination," J. Phys. D: Appl. Phys. **44**(22), 224011 (2011).

[6]P. Béquin, A. N. Tonlio, and S. Durand, "Air plasma sensor for the measurement of sound pressure using millimetric and micrometric discharges," J. Appl. Phys. **127**(3), 034502 (2020).

[7]G. E. Georghiou, A. P. Papadakis, R. Morrow, and A. C. Metaxas, "Numerical modelling of atmospheric pressure gas discharges leading to plasma production," J. Phys. D: Appl. Phys. **38**(20), R303 (2005).

[8]F. F. Wu, R. Liao, L. J. Yang, X. H. Liu, K. Wang, and Z. Zhou, "Numerical simulation of Trichel pulse characteristics in bar-plate DC negative corona discharge," Acta Phys. Sin. **62**(11), 115201 (2013).

[9]Y. S. Zheng, L. J. Wang, D. Wang, and S. L. Jia, "Numerical study of the effect of the needle tip radius on the characteristics of Trichel pulses in negative corona discharges," Phys. Plasmas **24**, 063515 (2017).

[10]B. X. Lu, H. Y. Sun, and Q. K. Wu, "Characteristics of Trichel pulse parameters in negative corona discharge," IEEE Trans. Plasma Sci. **45**(8), 2191–2201 (2017).

[11]B. X. Lu, H. Y. Sun, Y. Yang, and Q. K. Wu, "The role of negative corona in charged particle dynamics," Simul. Modell. Practice Theory **74**, 64–79 (2017).

[12]P. Sattari, G. S. Peter Castle, and K. Adamiak, "Simulation of Trichel pulses in a negative corona discharge in air," IEEE Trans. Indus. Appl. **47**(4), 1935–1943 (2011).

[13]B. X. Lu and H. Y. Sun, "Ion-impact secondary emission in negative corona with photoionization," AIP Adv. **7**(3), 035002 (2017).

[14]H. Y. Sun, S. L. Huang, Q. Wang, S. Wang, and W. Zhao, "Characteristics of negative corona discharge in air at various gaps," IEEE Trans. Plasma Sci. **47**(1), 736–741 (2019).

[15]Q. Feng, S. Zhong, M. Zheng, and Z. Dang, "Numerical study of negative corona discharge characteristics at different electrode gap spacing," IEEE Trans. Plasma Sci. **48**(8), 2831–2836 (2020).

[16]Z. Liu, T. Liu, X. Miao, W. Guo, and S. He, "Experimental research on spectral intensity of needle-plate corona discharge," J. Phys.: Conf. Ser. **418**, 012105 (2013).

[17]R. Tirumala, Y. Li, D. A. Pohlman, and D. B. Go, "Corona discharges in sub-millimeter electrode gaps," J. Electrostatics **69**(1), 36–42 (2011).

[18]J. S. Jung and J. D. Moon, "Corona discharge and ozone generation characteristics of a wire-plate discharge system with a glass-fiber layer," J. Electrostatics **66**(5), 335–341 (2008).

[19]J. P. Borra, "Review on water electro-sprays and applications of charged drops with focus on the corona-assisted cone-jet mode for high efficiency air filtration by wet electro-scrubbing of aerosols," J. Aerosol Sci. **125**, 208–236 (2018).

[20]A. Venkattraman and A. A. Alexeenko, "Scaling law fordirect current field emission-driven microscale gasbreakdown," Phys. Plasmas **19**, 123515 (2021).

[21]G. Meng, J. She, Q. Ying, X. Gao, and Y. Cheng, "Research progress on numerical simulation of gas breakdown at microscale," Trans. China Electrotechnical Soc. **37**(15), 3857–3875 (2022).

[22]W. S. Kang, J. M. Park, Y. Kim, and S. H. Hong, "Numerical study on influences of barrier arrangements on dielectric barrier discharge characteristics," IEEE Trans. Plasma Sci. **31**(4), 504–510 (2003).

[23]O. Ducasse, L. Papageorghiou, O. Eichwald, N. Spyrou, and M. Yousfi, "Critical analysis on two-dimensional point-to-plane streamer simulations using the finite element and finite volume methods," IEEE Trans. Plasma Sci. **35**(5), 1287–1300 (2007).